



Single-crystal TiO₂/SrTiO₃ core–shell heterostructured nanowire arrays for enhanced photoelectrochemical performance

Ying Chen, Shi Li, Ruo-Yu Zhao, Wei Li, Zhao-Hui Ren* , Gao-Rong Han

Received: 8 December 2018 / Revised: 28 December 2018 / Accepted: 22 January 2019 / Published online: 4 March 2019
© The Nonferrous Metals Society of China and Springer-Verlag GmbH Germany, part of Springer Nature 2019

Abstract Vertically aligned TiO₂/SrTiO₃ core–shell heterostructured nanowire arrays with different shell thicknesses (5–40 nm) were fabricated on fluorine-doped tin oxide substrate via a hydrothermal process. Microstructural characterization demonstrated that the TiO₂ nanowires were uniformly coated by the single-crystal SrTiO₃ shell, where continuous and large-area interface could be clearly observed. By this means, significantly enhanced photoelectrochemical water splitting properties (0.78 mA·cm⁻² at 1.23 V vs. RHE) were successfully realized in well-designed sample (with a shell thickness of 5–10 nm) compared with those of pristine TiO₂ (0.38 mA·cm⁻² at 1.23 V vs. RHE). The improvement of photoelectrochemical properties was attributed to the improved charge injection and charge separation, which are calculated by the results of water oxidation and sulfite oxidation measurements. Based on these results, a mechanism was proposed that SrTiO₃ shell acted as an electron–hole separation layer to improve the photocurrent density. On the other hand, the sample with an over-thick SrTiO₃ shell (20–40 nm) exhibited slightly reduced photoelectrochemical properties (0.66 mA·cm⁻²), which could be explained by the increase of the recombination rate in the

thicker SrTiO₃ shell. This work provided a facile strategy to improve and modulate the photoelectrochemical performance of heterostructured photoanodes.

Keywords TiO₂/SrTiO₃ heterostructured nanowire arrays; Photoelectrochemical water splitting; Shell thickness; Band alignment

1 Introduction

Hydrogen generation through solar energy has been extensively considered as a favorable method to solve the global energy crisis due to its clean, renewable and environment-friendly character [1]. Up to now, numerous efforts have been made to realize solar-driven water splitting in a low-cost and high-efficient way [2, 3]. Photoelectrochemical (PEC) water splitting, because of its high efficiency and high reliability, shows a promising application prospect for hydrogen production and therefore is attracting widespread attention of the researchers [4–6]. On the basis of the previous studies, N-type semiconductor transition-metal oxides, such as titanium dioxide (TiO₂) [7–9], zinc oxide (ZnO) [10, 11], and tungsten trioxide (WO₃) [12–14] could be used as photoanode materials for PEC water splitting. In particular, TiO₂ has been widely investigated as an important photoanode material due to its suitable conducting band (CB) level, strong ultraviolet (UV) absorption, superior chemical stability and low cost [15, 16]. It has been proved that one-dimensional vertically aligned TiO₂ arrays exhibit even higher PEC performance, which could be a result of large surface area and effective charge transfer due to its specific microstructure [17, 18]. However, there still remain some issues that would

Electronic supplementary material The online version of this article (<https://doi.org/10.1007/s12598-019-01221-6>) contains supplementary material, which is available to authorized users.

Ying Chen and Shi Li have contributed equally to this article.

Y. Chen, S. Li, R.-Y. Zhao, W. Li, Z.-H. Ren*, G.-R. Han
State Key Laboratory of Silicon Materials, School of Materials
Science and Engineering, Cyrus Tang Center for Sensor
Materials and Application, Zhejiang University, Hangzhou
310027, China
e-mail: renzh@zju.edu.cn

substantially limit the PEC performance of TiO₂, including large band gap and high electron–hole recombination rate [5, 19, 20]. Toward these issues, fascinating strategies have been developed of TiO₂-based photoanodes, including doping [21, 22], surface treatment [7] and fabricating heterostructured nanocomposites [23–26].

Particularly, it has been verified that fabricating heterostructured nanocomposites is a facile and efficient approach to significantly enhance the PEC performance of TiO₂-based photoanodes [3]. This could be attributed to the fact that the heterostructure constituted by two suitable semiconductors could improve the light absorption, facilitate photo-induced charge separation and increase the surface charge injection efficiency [27]. To date, numerous photocatalysts with a promising visible light absorption or charge injection, such as CdS [28, 29], BiVO₄ [25], Fe₂O₃ [30, 31] and g-C₃N₄ [32] were applied to the TiO₂-based photoanodes as the photoactive reaction sites. Moreover, strontium titanate (SrTiO₃, STO) was also reported to be a preferable photocatalyst for both pollutant degradation [33, 34] and water splitting [35–37], and various TiO₂/STO heterostructured photoanodes have been investigated to demonstrate an enhanced PEC performance [38, 39]. In these photoanodes, TiO₂ mainly acts as the provider and transport path of the photo-generated electrons and holes, while STO acts as the injection path of the photo-generated holes. Previous reports have confirmed that a heterostructure constituted by two single-crystal components with high-quality interface could efficiently facilitate charge separation, and therefore increase the photocatalytic properties [3]. However, the TiO₂ core in these photoanodes is polycrystalline and constituted by aggregated particles [38, 39], thus limiting the formation of the large-area, continuous and high-quality TiO₂/STO interface. More importantly, the effect of shell thickness on PEC performance in the core–shell heterostructured photoanodes has rarely been investigated due to the difficulties in the synthesis and characterization of the core–shell heterojunction with different shell thicknesses.

In this work, single-crystal core–shell TiO₂/STO nanowire arrays were synthesized via a two-step hydrothermal method. According to the experiment result, well-designed core–shell TiO₂/STO nanowire arrays (NAs) photoanode displayed enhanced photoelectrochemical performance compared to pristine TiO₂ NAs. This result is attributed to the promotion of charge separation efficiency and injection efficiency, which could further originate from the proper band alignment between TiO₂ and STO. This work demonstrates that fabrication of core–shell heterojunction with large interface area could be an efficient strategy to improve PEC water splitting, where the shell thickness is suggested to be an important factor to modulate the PEC

performance by influencing charge separation efficiency and injection efficiency.

2 Experimental

2.1 Preparation of TiO₂/SrTiO₃ nanowire arrays

First, rutile TiO₂ NAs were prepared on fluorine-doped tin oxide (FTO) substrate via a facile hydrothermal process. 15 ml deionized water was mixed with 15 ml concentrated hydrochloric acid (36.5 wt%–38.0 wt%). The mixture was stirred for 1 min and then transferred into a 50 ml Teflon-lined stainless-steel autoclave. Subsequently, 0.5 ml tetrabutyl titanate (TBOT) was added into the mixture under continuous stirring. One piece of FTO glass substrate (1.5 cm × 3.0 cm), which was cleaned via ultrasonic washing for 15 min in the mixture solution of deionized water, acetone and isopropyl alcohol (1:1:1), was placed at an angle against the wall of the reactor with the conducting side facing down. Hydrothermal process was performed at 150 °C for 8 h. After cooling down to room temperature, the FTO substrate was washed with deionized water several times to remove the residual hydrochloric acid and TBOT and dried at room temperature naturally.

Core–shell TiO₂/SrTiO₃ NAs with different shell thicknesses were prepared by a second hydrothermal process, where TiO₂ NAs were set to be the templates. Firstly, different amounts of Sr(OH)₂·8H₂O were dissolved in 20 ml deionized water to obtain the solution with the concentration of 0, 0.005, 0.020, 0.050, 0.100 mol·L⁻¹, respectively. And the obtained solution was then transferred into a 50 ml Teflon-lined stainless-steel autoclave. The as-prepared TiO₂ NAs substrate was placed at an angle against the wall with TiO₂ NAs facing down. Hydrothermal process was performed at 200 °C for 8 h. After cooling down to room temperature, the substrate was washed with deionized water and 3 wt% hydrochloric acid to remove the residual Sr(OH)₂·8H₂O and then dried at 60 °C in air. Finally, to improve the crystallinity of NAs, the substrate was annealed at 450 °C in air for 1 h.

2.2 Characterization techniques

X-ray diffraction (XRD) patterns were carried out at room temperature using a Thermo ARL X'TRA diffractometer with Bragg–Brentano geometry by Cu K α radiation ($\lambda = 0.154056$ nm) under 0.082-nm resolution. The morphology was investigated using a scanning electron microscope (SEM, Zeiss and Hitachi MODEL SU-70) with an accelerating voltage of 5 kV. Transmission electron microscopy (TEM) and high-resolution TEM (HRTEM) images were taken by FEI Technai G² F20 operated at the

accelerating voltage of 200 kV and the bias voltage of 3950 V, which was combined with energy dispersive X-ray (EDX) spectroscopy. Solid ultraviolet–visible (UV–Vis) diffuse reflection spectra were collected on Agilent Cary 5000 UV–Vis–NIR spectrophotometer with integrating sphere.

2.3 Photoelectrochemical measurements

All PEC tests were performed on an electrochemical workstation (CHI 660e, CH Instruments Inc., Shanghai) in a three-electrode configuration, where Pt sheet works as the counter electrode and Ag/AgCl electrode works as the reference electrode. All electrodes were drossed in an alkaline medium of a 1 mol·L⁻¹ NaOH aqueous solution (pH = 14). The illumination source was a 300-W Xe lamp under AM 1.5G light filter with a power density of 100 mW·cm⁻² on the photoanode. The conducting wire was soldered to FTO substrate by soldering tin and metallic indium to form the photoanode. The working, counter and reference electrodes were installed in a quartz cell. The photocurrent was measured by liner sweep voltammetry at a scan rate of 20 mV·s⁻¹. The photoconversion efficiency (η) was calculated using the following equation:

$$\eta = J \times (1.23 - E_{\text{RHE}}) / P_{\text{light}} \quad (1)$$

where E_{RHE} is the applied bias versus reversible hydrogen electrode (RHE), J is the photocurrent density at the measured bias and P_{light} is the irradiance intensity of 100 mW·cm⁻². The E_{RHE} was calculated by:

$$E_{\text{RHE}} = E_{\text{Ag/AgCl}} + E_{\text{Ag/AgCl}}^{\theta} + 0.059 \text{ pH} \quad (2)$$

where $E_{\text{Ag/AgCl}}$ is the applied bias versus Ag/AgCl and $E_{\text{Ag/AgCl}}^{\theta}$ is the standard electrode potential of the Ag/AgCl (0.2224 V at 25 °C). Electrochemical impedance spectroscopy (EIS) was carried out by applying an alternative current (AC) voltage at -0.4 V in a frequency range from 100 kHz to 0.01 Hz under illumination. Mott–Schottky plots were evaluated at a direct current (DC) potential range from -1.5 to 0 V at a frequency of 1 kHz.

3 Result and discussion

3.1 Material characterization

The schematic illustration of the fabrication of TiO₂ and TiO₂/STO NAs on FTO substrate is shown in Fig. 1a. Vertically aligned precursors of TiO₂ NAs were firstly grown on a FTO substrate via a hydrothermal process. Subsequently, the second hydrothermal process using Sr(OH)₂ was employed to convert the surface of TiO₂ NAs

into STO. Finally, the precursor was annealed to acquire TiO₂ and TiO₂/STO NAs on FTO substrate. The samples synthesized by different concentrations of Sr(OH)₂ in second hydrothermal process are denoted as TiO₂ (0 mol·L⁻¹), STO0.005 (0.005 mol·L⁻¹), STO0.020 (0.020 mol·L⁻¹), STO0.050 (0.050 mol·L⁻¹) and STO0.100 (0.100 mol·L⁻¹) samples. XRD patterns of the samples are shown in Fig. 1b, where sharp peaks located at 26°, 38° and 52° could be detected in all patterns corresponding to SnO₂ in the FTO substrate (marked using a rectangle symbol). Besides, the diffraction peaks of rutile TiO₂ (JCPDS No. 88-1175) could be detected in all patterns, while the diffraction peaks of STO (JCPDS No. 35-0734) could only be detected in STO0.020, STO0.050 and STO0.100 samples. Obviously, the intensity of the peaks of STO increases along with the increase of the concentration of Sr(OH)₂, and meanwhile, the peaks of rutile TiO₂ diminish correspondingly. This result suggests that STO shell generates with the consumption of TiO₂ core, and higher concentration of Sr(OH)₂ could lead to more TiO₂ conversion. However, the STO0.005 sample shows no peaks corresponding to STO, which could be possibly attributed to the poor crystallinity and low content of STO.

Figure 1c–g show SEM images of TiO₂ NAs and TiO₂/STO core-shell heterostructured NAs (top view and cross-section view, respectively). It could be observed that all samples demonstrate a morphology of vertically aligned nanowires with regular facets on FTO substrate. The average length and diameter of pristine TiO₂ NAs are ~1.5 and ~100.0 nm, respectively (Fig. 1c). No significant size difference could be observed in STO coated samples (Fig. 1d–g). Differently, the nanowires in STO0.050 and STO0.100 samples (Fig. 1f, g) exhibit rough surface, and a few nanoparticles appear on the top side of the NAs. This morphology could possibly be attributed to the transition process from rutile TiO₂ to STO in the second hydrothermal process.

Figure 2 illustrates TEM and EDX mapping images of STO0.020 sample. The morphology of a typical TiO₂/STO heterostructured nanowire with a diameter of ~120 nm is shown in Fig. 2a. This single nanowire exhibits smooth surface and regular one-dimensional shape, agreeing well with SEM results, and the thickness of STO shell of STO0.020 sample could be determined as 5–10 nm according to the statistical results (Fig. S1). HRTEM image and corresponding fast Fourier transform (FFT) patterns (Fig. 2b) have also been adopted to investigate the microstructure near the TiO₂/STO interface. The intervals of lattice fringes are detected to be 0.278 nm (vertically), 0.273 nm (horizontally) above the interface and 0.294 nm (vertically), 0.318 nm (horizontally) below the interface, corresponding to STO (110), (110) plane and rutile TiO₂

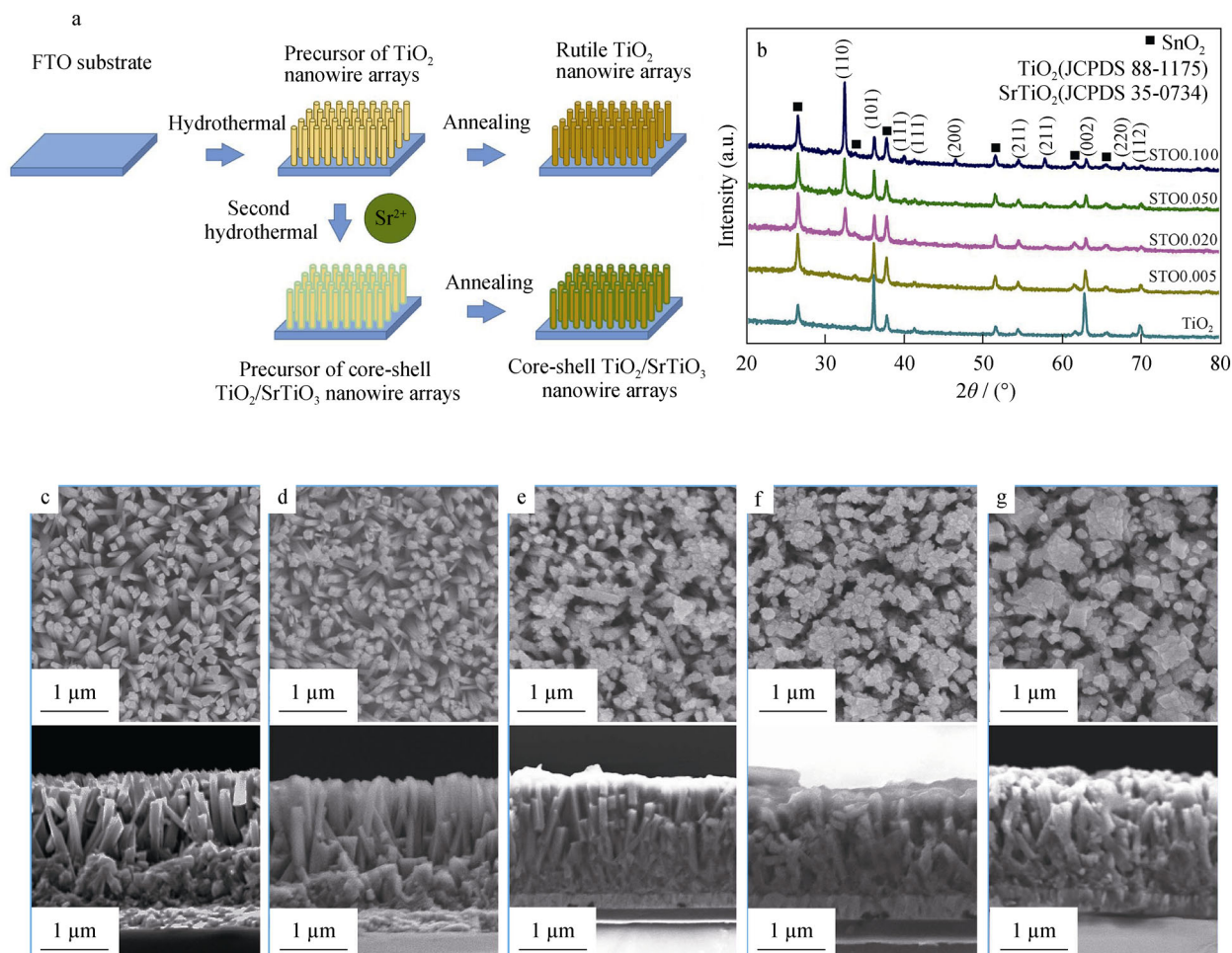


Fig. 1 **a** Schematic illustration of synthesis process of rutile TiO_2 NAs and core-shell TiO_2/STO NAs on FTO substrate; **b** XRD patterns; top-view and cross-section SEM images of **c** pristine TiO_2 NAs and **d** STO0.005, **e** STO0.020, **f** STO0.050 and **g** STO0.100 samples

(001), (110) planes, respectively. The calculated lattice mismatch is $\sim 6\%$, which is tolerable for a coherent interface. Besides, the insets show the FFT patterns corresponding to the area above and below the interface, respectively. Only one set of spots (along [001] zone axis of STO) could be observed in the FFT pattern of the area above the interface. As for the area below the interface, two sets of spots could be distinguished corresponding to STO [001] and TiO_2 $[1\bar{1}0]$ zone axis, respectively. This is probably because TiO_2 core is completely wrapped up with STO shell, and electron beams need to pass through the entire sample to obtain the image in TEM characterization. In addition, EDX elemental mapping (Fig. 2c, d) demonstrates the two-dimensional elemental distributions of Sr and Ti in the dashed-square marked region in Fig. 2a. As shown in Fig. 2c, d, Ti is uniformly distributed along the entire nanowire while Sr is concentrated at the edge of nanowire, suggesting a TiO_2/STO core-shell heterostructure with a shell thickness of ~ 10 nm. Meanwhile, STO0.100 sample was also characterized under TEM

(Fig. S2), showing a shell thickness of 20–40 nm. The nanowire of STO0.100 sample with a shell thickness of ~ 40 nm (Fig. S3) exhibits a rough surface (Fig. S3a), and a superposition area could be detected near the hetero-junction interface (Fig. S3b). HRTEM image indicates that the lattice spacing of the shell and core fits well with the (110)/(110) plane of STO and the (001)/(110) plane of rutile TiO_2 , respectively, similar to that of STO0.020 sample (Fig. S3b). In the FFT pattern of superposition area, two sets of spots can be distinguished corresponding to STO and rutile TiO_2 , respectively (Fig. S3d). And the particles on the tip of the nanowires are characterized to be well-crystallized STO (Fig. S3e–f). Accordingly, the results evidence that different concentrations of $\text{Sr}(\text{OH})_2$ in the reactant lead to a similar growth orientation, and the STO shell thickness increases as the $\text{Sr}(\text{OH})_2$ concentration rises. Based on this, it is reasonable to speculate that higher concentration of $\text{Sr}(\text{OH})_2$ in the reactant could lead to a thicker STO shell.

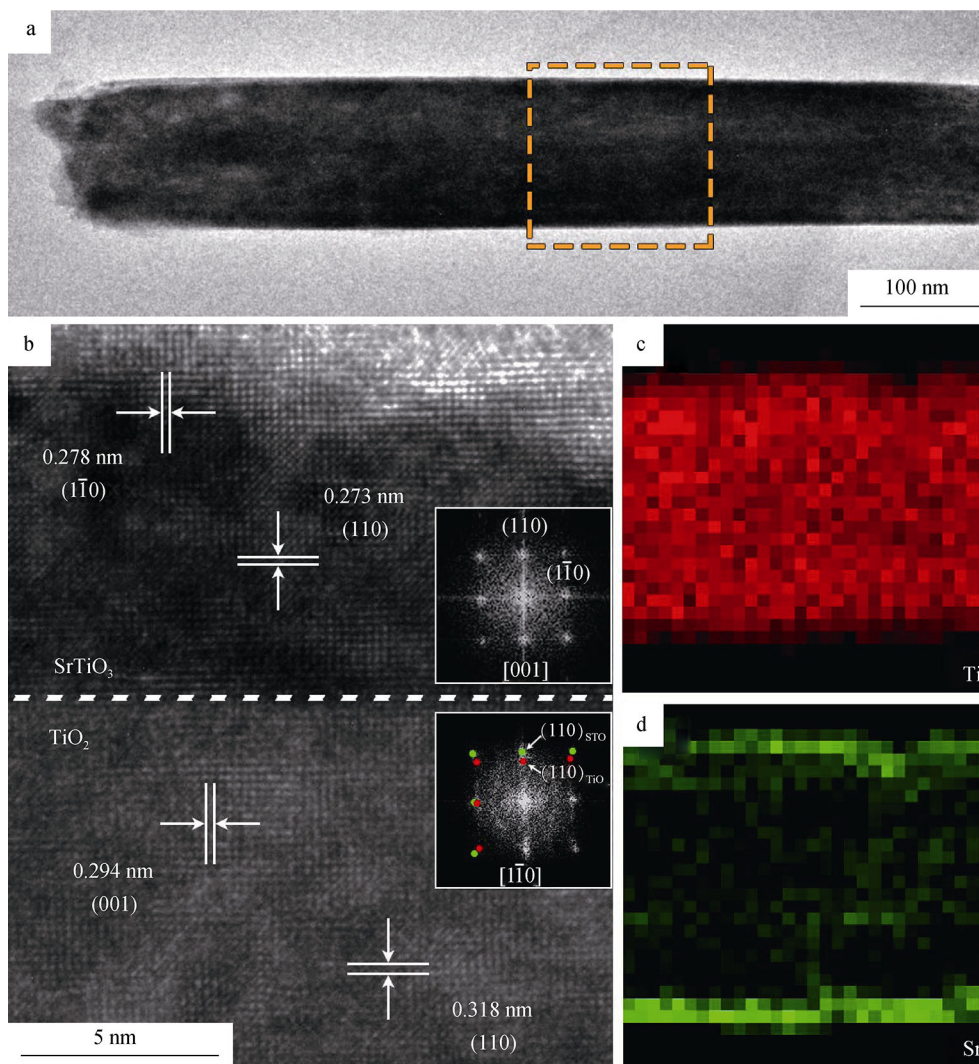


Fig. 2 Microstructure and elemental characterization of STO0.020 sample: **a** TEM image and **b** HRTEM image of a typical nanowire of STO0.020 sample (insets being corresponding FFT images corresponding to area above interface or below interface, respectively); EDX elemental mapping of dashed-square marked region in **a** with individual elements of **c** Ti (red) and **d** Sr (green)

3.2 PEC performance

The as-prepared pristine TiO₂ and TiO₂/STO core-shell heterostructured NAs were investigated as PEC photoanodes for water splitting under AM 1.5G illumination. Figure 3a shows the photocurrent density–potential (*I*–*V*) curves of pristine TiO₂ and core-shell TiO₂/STO NAs in 1 mol·L⁻¹ sodium hydroxide (NaOH) solution. According to the dark scan pattern, no obvious background current density can be detected, indicating that no electrochemical reaction occurs on PEC photoanodes. When the PEC photoanodes are under illumination, the current density quickly increases after the potential reaches 0.3–0.4 V (vs. RHE). The photocurrent density of pristine TiO₂ NAs at 1.23 V (vs. RHE) is 0.38 mA·cm⁻², while STO0.005 sample and STO0.020 sample show a photocurrent density

of 0.56 and 0.76 mA·cm⁻² (at 1.23 V vs. RHE), respectively, exhibiting 47% and 100% improvements compared to pristine TiO₂. As for STO0.050 and STO0.100 samples, the photocurrent density drops to 0.68 and 0.66 mA·cm⁻² at 1.23 V (vs. RHE), respectively. Furthermore, as the potential continues to increase after 1.23 V (vs. RHE), the photocurrent density tends to be stable, which could be resulted from the saturation of photo-generated carriers. Accordingly, the photoconversion efficiency has been calculated as a function of applied voltage (Fig. 3c) based on the results of photocurrent density. STO0.020 sample shows the maximum photoconversion efficiency of 0.18% at 0.82 V (vs. RHE), and other samples exhibit the lower value (TiO₂ 0.09%, STO0.005 0.15%, STO0.050 0.17% and STO0.100 0.15%), which demonstrate a similar variation with photocurrent density.

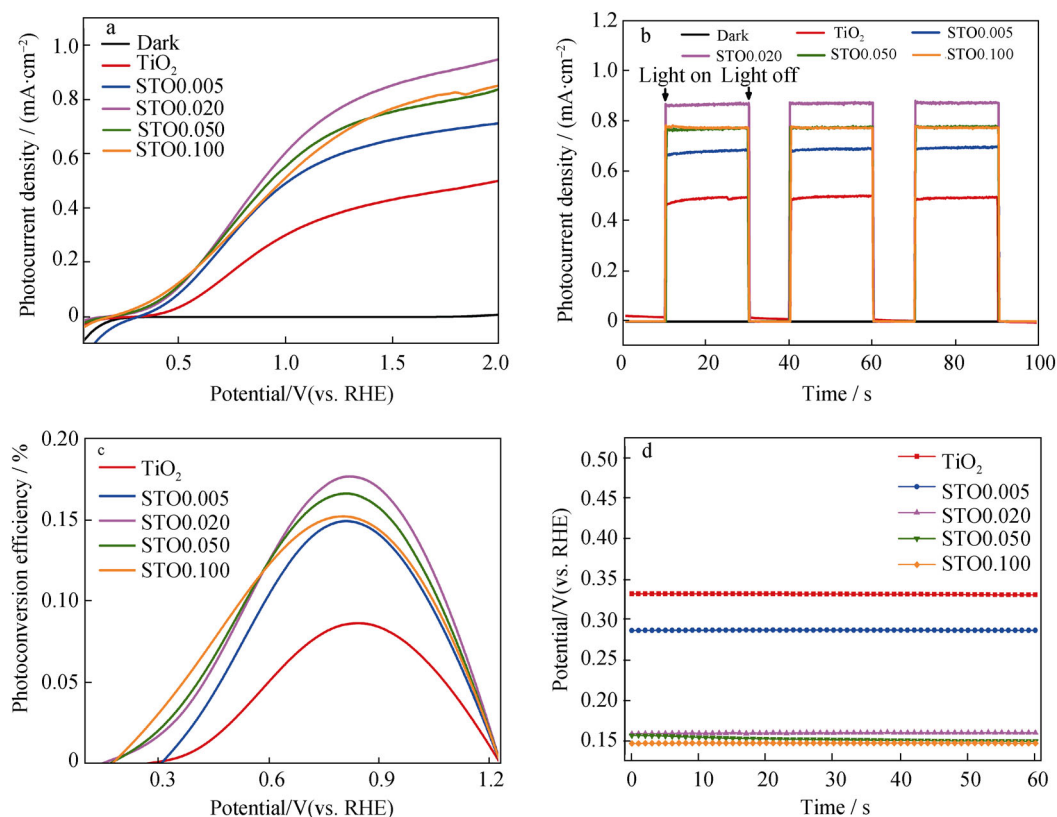


Fig. 3 PEC water oxidation performance of as-prepared TiO_2 and TiO_2/STO NAs photoanodes: **a** photocurrent density–voltage (J – V) curves, **b** amperometric I – t curves at potential of 1.5 V (vs. RHE) under chopped light illumination, **c** calculated photoconversion efficiency and **d** chronopotentiometric curves of TiO_2 and TiO_2/STO nanowire array photoanodes (all samples being measured in $1 \text{ mol}\cdot\text{L}^{-1}$ NaOH electrolyte under AM 1.5G illumination)

To investigate the photoresponse of pristine TiO_2 and TiO_2/STO core–shell heterostructured NAs, photocurrent–time (I – t) curves were carried out by chronoamperometry (Fig. 3b) under chopped light illumination at a stable potential of 1.5 V (vs. RHE). As shown in Fig. 3b, both pristine TiO_2 and TiO_2/STO core–shell heterostructured NAs display fast and reproducible photocurrent response with the light turns ON and OFF periodically. Meanwhile, the photocurrent density of the photoanodes under illumination is identical with that in J – V curves (at 1.5 V vs. RHE, Fig. 3a), which further demonstrates favorable photoresponse of the as-prepared photoanodes. Moreover, chronopotentiometric measurement with a constant current of zero has been taken to determine the change of onset potential. The onset potential reflects the surface band structure, which is effective to characterize the surface state of photoanodes. The result shows that the pristine TiO_2 , STO0.005 and STO0.020 samples exhibit declining onset potential (0.33, 0.28 and 0.17 V vs. RHE) with the increase of the $\text{Sr}(\text{OH})_2$ concentration in the reactant due to the continuous formation of STO shell. As for STO0.050 and STO0.100 samples, the onset potentials are 0.16 and 0.15 V (vs. RHE), respectively, indicating that there are

hardly any changes of surface state in the photoanodes compared with STO0.020 sample. Accordingly, it is suggested that TiO_2 NAs are completely wrapped in STO shell in STO0.020, STO0.050 and STO0.100 samples.

3.3 Mechanism discussion

According to the results of material characterization and PEC performance measurement, it is suggested that the photoanodes with a uniform STO shell could lead to largely improved PEC performance compared with pristine TiO_2 NAs, and STO shell thickness is vital in modulating the PEC performance. Theoretically, the photocurrent density can be described by the following relation:

$$J_{\text{PEC}} = J_{\text{abs}} \times \eta_{\text{separation}} \times \eta_{\text{injection}} \quad (3)$$

where J_{PEC} is measured photocurrent density, J_{abs} is theoretical photocurrent density at 100% internal quantum efficiency, and $\eta_{\text{separation}}$ and $\eta_{\text{injection}}$ are separation efficiency and injection efficiency, which represent the possibility of photo-generated holes migrating to the surface and the surface-reaching holes participating in specific electrochemical reactions, respectively [26]. To further

understand the improvement of photocurrent density, light absorption property, charge separation and injection measurement have been taken to study its internal mechanism.

Firstly, the UV–Vis light absorption spectra is obtained to investigate the influence of J_{abs} (Fig. S4), showing a same light absorption edge (~ 410 nm) of the pristine TiO₂ and core-shell TiO₂/STO NAs. According to the previous report, only light with the wavelength under 420 nm could be well utilized by rutile TiO₂ and STO, thus the light absorption over 300–420 nm is worth a strong attention (the intensity of light with the wavelength under 300 nm is too weak to consider according to AM 1.5G solar spectrum in Fig. S5b) [7]. According to absorption plus scattering (A + S) spectrum (Fig. S5a), AM 1.5G solar spectrum (Fig. S5b) and light harvesting efficiency (LHE) spectrum (Fig. S5c), the maximum electron flux at the photoanodes was successfully calculated (Fig. S5d), achieving the J_{abs} values of 1.47, 1.49, 1.46, 1.46 and 1.44 mA·cm⁻² corresponding to pristine TiO₂, STO0.005, STO0.020, STO0.050 and STO0.100 samples, respectively. The calculated J_{abs} shows tiny variation so as to be ignored, which demonstrates that light absorption should not take any responsibility for the improvement of PEC performance.

To investigate the influence of $\eta_{\text{separation}}$ and $\eta_{\text{injection}}$, PEC sulfite oxidation (SO) and water oxidation (WO) measurements were adopted, where phosphate buffer solution (pH = 7) with and without sodium sulfite was used as electrolytes, respectively. As reported before, sodium sulfite is considered as a strong hole scavenger. In the process of SO, $\eta_{\text{injection}}$ can be approximated as 100% [40], thus, the relation can be described as:

$$J_{\text{SO}} = J_{\text{abs}} \times \eta_{\text{separation}} \quad (4)$$

where J_{SO} is the photocurrent density of SO; thus, $\eta_{\text{separation}}$ can be calculated easily ($\eta_{\text{separation}} = J_{\text{SO}}/J_{\text{abs}}$). Then according to photocurrent density of WO, $\eta_{\text{injection}}$ can be calculated by the relation as:

$$\eta_{\text{injection}} = J_{\text{WO}}/(J_{\text{abs}} \times \eta_{\text{separation}}) \quad (5)$$

Figure 4a, b shows the results of SO and WO measurement, respectively. It could be observed that all core-shell TiO₂/STO NAs show higher photocurrent density than pristine TiO₂ by both WO and SO measurements, similar to the results of PEC photocurrent density measured in sodium hydroxide electrolyte. However, the value of photocurrent density of SO is much higher than that of WO in the same sample, which is caused by the obvious improvement of $\eta_{\text{injection}}$ in sodium sulfite electrolyte. According to the equation above, $\eta_{\text{separation}}$ and $\eta_{\text{injection}}$ are calculated and shown in Fig. 4c, d. It can be observed that STO0.020 sample shows substantially improved $\eta_{\text{separation}}$ and $\eta_{\text{injection}}$ ($\sim 59\%$ and $\sim 100\%$ at 1.23 V vs. RHE)

compared with pristine TiO₂ NAs ($\sim 37\%$ and $\sim 83\%$ at 1.23 V vs. RHE), which exhibit 59.4% and 20.5% enhancement, respectively. Meanwhile, the insets clearly show the variation trend of $\eta_{\text{separation}}$ and $\eta_{\text{injection}}$ with the increase of Sr(OH)₂ concentration in the reactant. As the Sr(OH)₂ concentration in the reactant increases, $\eta_{\text{separation}}$ and $\eta_{\text{injection}}$ first increase (STO0.005 and STO0.020) and then reduce (STO0.050 and STO0.100), agreeing well with the variation of photocurrent density. The results of the SO and WO measurement indicate that both improved injection efficiency and separation efficiency should take the responsibility for enhanced PEC performance.

To reveal the specific mechanism of improved $\eta_{\text{separation}}$ and $\eta_{\text{injection}}$, light absorption property, charge carrier density, charge transport resistance and band structure should be taken into consideration. First of all, the light absorption has been discussed before (Figs. S4 and S5), which shows no variation between pristine TiO₂ and TiO₂/STO core-shell heterostructured samples. Secondly, electrochemical impedance measurements have been employed in order to investigate the influence of charge carrier density and charge transport resistance. Figure S6a shows the Mott–Schottky plots of the as-prepared pristine TiO₂ and core-shell TiO₂/STO NAs photoanodes. The positive slope of the plots indicates that all samples are *n*-type semiconductor. According to Mott–Schottky equation, the charge carrier density is calculated from the slope, which is 2.31×10^{19} , 2.03×10^{19} , 1.19×10^{19} , 2.25×10^{19} and 4.00×10^{19} cm⁻³ corresponding to pristine TiO₂, STO0.005, STO0.020, STO0.050 and STO0.100 samples, respectively [14, 41, 42]. The slight difference of the charge carrier density among the samples suggests that STO shell could hardly improve the carrier density of the samples. Accordingly, the charge carrier density should not be the reason for enhanced PEC performance.

The electrochemical impedance spectroscopy (EIS) plots are shown in Fig. S6b. It is obvious that the pristine TiO₂ NAs show the smallest semicircle diameter among the samples, corresponding to the lowest charge transport resistance. As for STO0.005, STO0.020, STO0.050 and STO0.100 samples, the semicircle diameter slightly improves as the STO shell becomes thicker, indicating an improved charge transport resistance. This phenomenon could be explained by the poor charge transport properties of STO compared with rutile TiO₂ and the barrier in the TiO₂/STO interface, suggesting that charge transport is not the reason for enhanced PEC performance.

Band structure of the core-shell TiO₂/STO NAs and the schematic illustration of the carrier transfer process in core-shell TiO₂/STO NAs photoanodes are shown in Fig. 5a, b, respectively [43]. As shown in Fig. 5a, the conductive band of TiO₂ is located at 0.15 V, higher than that of STO (-0.12 V). In the interface of TiO₂/STO,

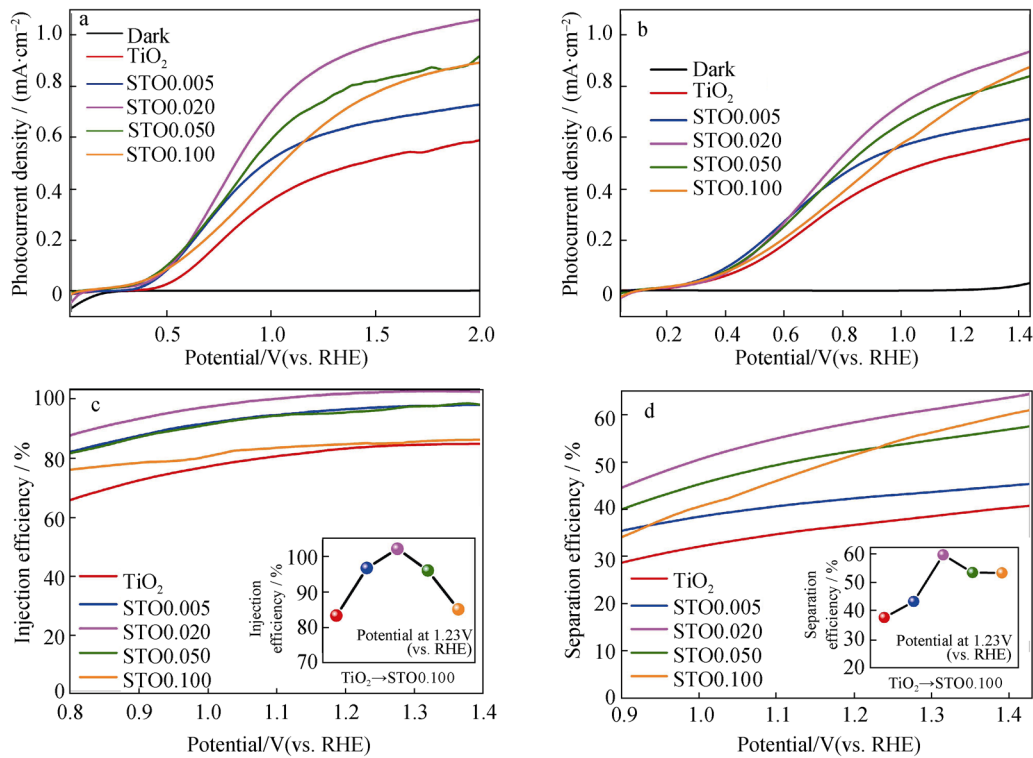


Fig. 4 Photocurrent density–voltage (J – V) curves of pristine TiO_2 and TiO_2/STO nanowire array photoanodes for **a** SO measured in $0.5 \text{ mol}\cdot\text{L}^{-1}$ phosphate buffer with $1 \text{ mol}\cdot\text{L}^{-1}$ Na_2SO_3 ($\text{pH} = 7$) as hole scavenger and **b** WO measured in $0.5 \text{ mol}\cdot\text{L}^{-1}$ phosphate buffer ($\text{pH} = 7$) under AM 1.5 G illumination; Calculated efficiency of **c** charge injection and **d** charge separation of photoanodes (insets showing variation trend of calculated efficiency)

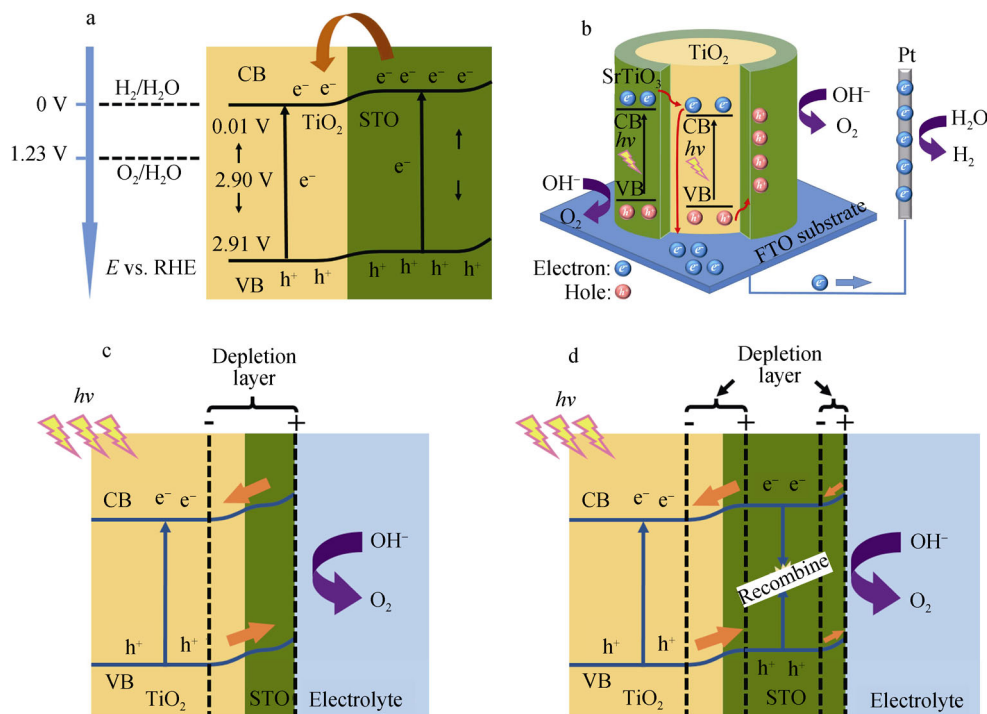


Fig. 5 **a** Band diagram of TiO_2/STO heterojunction; **b** a schematic illustration of PEC water oxidation process in TiO_2/STO nanowire array photoanodes; **c**, **d** variation of surface states in photoanodes with different STO shell thicknesses

photo-generated electrons flow from STO shell to TiO₂ core spontaneously due to the difference between the energy levels (Fig. 5a). Meanwhile, the photo-generated holes flow from TiO₂ core to STO shell, forming a depletion layer in the interface ultimately, which reduces the possibility of the recombination of photo-generated electrons and holes. The space charge transfer process is shown in Fig. 5b. The electrons in the valence band are inspired by the light and jump into the conductive band. This process both occurs in STO shell and TiO₂ core at the same time. Owing to the band alignment between TiO₂ and STO, the photo-generated electrons and holes start to migrate directionally, leading to aggregation of electrons in TiO₂ and holes in STO. Then the electrons in TiO₂ are transferred to counter electrode under the effect of bias voltage for water reduction, and the holes in STO react in the surface of photoanodes for water oxidation. Therefore, the proper band structure and resulting depletion layer in TiO₂/STO interface are the main reason for the increase of $\eta_{\text{separation}}$ compared with pristine TiO₂ NAs photoanode.

Moreover, the mechanism illustration of the dropped $\eta_{\text{separation}}$ of STO0.100 sample compared with that of STO0.020 sample is shown in Fig. 5c, d. In STO0.020 sample, the depletion layer in the TiO₂/STO interface is very close to the band bending near electrode/electrolyte interface (Fig. 5c) because of the low thickness of the STO shell (5–10 nm). As a result, the STO shell plays the role of an electron–hole separation layer, where electrons and holes will quickly migrate to the opposite sides of STO shell. In this case, the concentration of the carriers is relatively low, which promotes the separation of photo-generated electrons–holes pairs and reduces the possibility of recombination (Fig. 5c). However, when the STO shell thickness increases to more than 20 nm (STO0.050 and STO0.100 samples), the STO shell is more like bulk material. The internal band structure tends to flatten, leading to low charge carrier transport efficiency. This could improve the possibility of recombination of the electron–hole pairs during the charge carrier transport process in STO shell (Fig. 5d). Therefore, the STO0.050 and STO0.100 samples (with a thick STO shell of over 20 nm), on the contrary, show a reduced $\eta_{\text{separation}}$ compared to STO0.020 (with a STO shell of 5–10 nm) samples.

In addition, the variation of $\eta_{\text{injection}}$ could be explained by the change of surface microstructure. First of all, the increased $\eta_{\text{injection}}$ of STO0.020 sample compared to pristine TiO₂ is possibly attributed to the rebuilding of crystal structures in the surface of photoanodes during the second hydrothermal process. The process that rutile TiO₂ in the surface transforms into STO could lead to a better crystallinity of the photoanode surface, therefore giving rise to an increased $\eta_{\text{injection}}$. As for STO0.050 and STO0.100 samples, it could be speculated that the STO particles on

the tip of the NAs (Fig. S3e, f) could influence the mass transfer efficiency at electrode/electrolyte interface, and the rough surface (Fig. S3a, b) of the nanowires could also form a barrier of the carrier injection, leading to the decline of $\eta_{\text{injection}}$ compared to STO0.020 sample.

4 Conclusion

In summary, TiO₂/STO core–shell heterostructured NAs photoanode with difference STO shell thicknesses were fabricated by a two-step hydrothermal process. According to experiment results, STO0.020 sample, where the STO shell was characterized to be 5–10 nm, yield the highest photocurrent density (0.78 mA·cm⁻² at 1.23 V vs. RHE), which is 1.82 times that in pristine TiO₂ (0.36 mA·cm⁻² at 1.23 V vs. RHE). As the STO shell thickness increased to over 20 nm in STO0.050 and STO0.100 samples, the as-prepared photoanodes show a slight drop PEC performance (0.68 and 0.66 mA·cm⁻² at 1.23 V vs. RHE) compared to STO0.020 sample. The variation of PEC properties is attributed to the charge injection and charge separation, which is calculated by the results of WO and SO measurements. Based on the experimental results, a mechanism has been proposed to explain the results, where the surface microstructure and band structure could be inferred as the reason of the variation of charge injection and charge separation efficiency, respectively. This work provides a new strategy to modulate the PEC properties by adjusting the shell thickness of the core–shell heterostructure, which could be inspiring to guide the design of the heterostructured photoanodes.

Acknowledgements This work was financially supported by the National Natural Science Foundation of China (Nos. 51232006, 51472218 and 11474249) and the National Basic Research Program of China (No. 2015CB654900).

References

- [1] Chow J, Kopp RJ, Portney PR. Energy resources and global development. *Science*. 2003;302(5650):1528.
- [2] Maeda K, Domen K. Photocatalytic water splitting: recent progress and future challenges. *J Phys Chem Lett*. 2010;1(18):2655.
- [3] Kudo A, Miseki Y. Heterogeneous photocatalyst materials for water splitting. *Chem Soc Rev*. 2009;38(1):253.
- [4] Gratzel M. Photoelectrochemical cells. *Nature*. 2001;414:338.
- [5] Hisatomi T, Kubota J, Domen K. Recent advances in semiconductors for photocatalytic and photoelectrochemical water splitting. *Chem Soc Rev*. 2014;43(11):7520.
- [6] Chen YZ, Li WH, Li L, Wang LN. Progress in organic photocatalysts. *Rare Met*. 2018;37(1):1.
- [7] Wang G, Wang H, Ling Y, Tang Y, Yang X, Fitzmorris RC, Wang C, Zhang JZ, Li Y. Hydrogen-treated TiO₂ nanowire

- arrays for photoelectrochemical water splitting. *Nano Lett.* 2011;11(7):3026.
- [8] Wang W, Dong J, Ye X, Li Y, Ma Y, Qi L. Heterostructured TiO₂ nanorod@nanobowl arrays for efficient photoelectrochemical water splitting. *Small.* 2016;12(11):1469.
 - [9] Wang Y, Zhang YY, Tang J, Wu H, Xu M, Peng Z, Gong XG, Zheng G. Simultaneous etching and doping of TiO₂ nanowire arrays for enhanced photoelectrochemical performance. *ACS Nano.* 2013;7(10):9375.
 - [10] Wolcott A, Smith WA, Kuykendall TR, Zhao Y, Zhang JZ. Photoelectrochemical study of nanostructured ZnO thin films for hydrogen generation from water splitting. *Adv Funct Mater.* 2009;19(12):1849.
 - [11] Yang X, Wolcott A, Wang G, Sobo A, Fitzmorris RC, Qian F, Zhang JZ, Li Y. Nitrogen-doped ZnO nanowire arrays for photoelectrochemical water splitting. *Nano Lett.* 2009;9(6):2331.
 - [12] Cristino V, Caramori S, Argazzi R, Meda L, Marra GL, Bignozzi CA. Efficient photoelectrochemical water splitting by anodically grown WO₃ electrodes. *Langmuir.* 2011;27(11):7276.
 - [13] Liu X, Wang F, Wang Q. Nanostructure-based WO₃ photoanodes for photoelectrochemical water splitting. *Phys Chem Chem Phys.* 2012;14(22):7894.
 - [14] Li W, Da P, Zhang Y, Wang Y, Lin X, Gong X, Zheng G. WO₃ nanoflakes for enhanced photoelectrochemical conversion. *ACS Nano.* 2014;8(11):11770.
 - [15] Fujishima A, Honda K. Electrochemical photolysis of water at a semiconductor electrode. *Nature.* 1972;238(5358):37.
 - [16] Bak T, Nowotny J, Rekas M, Sorrell CC. Photo-electrochemical hydrogen generation from water using solar energy. Materials-related aspects. *Int J Hydrog Energy.* 2002;27(10):991.
 - [17] Zhu K, Neale NR, Miedaner A, Frank AJ. Enhanced charge-collection efficiencies and light scattering in dye-sensitized solar cells using oriented TiO₂ nanotubes arrays. *Nano Lett.* 2007;7(1):69.
 - [18] Roy P, Berger S, Schmuki P. TiO₂ nanotubes: synthesis and applications. *Angew Chem Int Ed.* 2011;50(13):2904.
 - [19] Li Y, Zhang JZ. Hydrogen generation from photoelectrochemical water splitting based on nanomaterials. *Laser Photonics Rev.* 2010;4(4):517.
 - [20] Chen Z, Jaramillo TF, Deutsch TG, Kleiman-Shwarscstein A, Forman AJ, Gaillard N, Garland R, Takanabe K, Heske C, Sunkara M, McFarland EW, Domen K, Miller EL, Turner JA, Dinh HN. Accelerating materials development for photoelectrochemical hydrogen production: standards for methods, definitions, and reporting protocols. *J Mater Res.* 2010;25(1):3.
 - [21] Hoang S, Guo S, Mullins CB. Coincorporation of N and Ta into TiO₂ nanowires for visible light driven photoelectrochemical water oxidation. *J Phys Chem C.* 2012;116(44):23283.
 - [22] Xu M, Da P, Wu H, Zhao D, Zheng G. Controlled Sn-doping in TiO₂ nanowire photoanodes with enhanced photoelectrochemical conversion. *Nano Lett.* 2012;12(3):1503.
 - [23] Ning F, Shao M, Xu S, Fu Y, Zhang R, Wei M, Evans DG, Duan X. TiO₂/graphene/NiFe-layered double hydroxide nanorod array photoanodes for efficient photoelectrochemical water splitting. *Energy Environ Sci.* 2016;9(8):2633.
 - [24] Pu YC, Wang G, Chang KD, Ling Y, Lin YK, Fitzmorris BC, Liu CM, Lu X, Tong Y, Zhang JZ, Hsu YJ, Li Y. Au nanostructure-decorated TiO₂ nanowires exhibiting photoactivity across entire UV-visible region for photoelectrochemical water splitting. *Nano Lett.* 2013;13(8):3817.
 - [25] Resasco J, Zhang H, Kornienko N, Becknell N, Lee H, Guo J, Briseno AL, Yang P. TiO₂/BiVO₄ nanowire heterostructure photoanodes based on type II band alignment. *ACS Cent Sci.* 2016;2(2):80.
 - [26] Yang W, Yu Y, Starr MB, Yin X, Li Z, Kvit A, Wang S, Zhao P, Wang X. Ferroelectric polarization-enhanced photoelectrochemical water splitting in TiO₂-BaTiO₃ core-shell nanowire photoanodes. *Nano Lett.* 2015;15(11):7574.
 - [27] Wetchakun N, Chaiwichain S, Inceesungvorn B, Pingmuang K, Phanichphant S, Minett AI, Chen J. BiVO₄/CeO₂ nanocomposites with high visible-light-induced photocatalytic activity. *ACS Appl Mater Interfaces.* 2012;4(7):3718.
 - [28] Sun WT, Yu Y, Pan HY, Gao XF, Chen Q, Peng LM. CdS quantum dots sensitized TiO₂ nanotube-array photoelectrodes. *J Am Chem Soc.* 2008;130(4):1124.
 - [29] Luo J, Ma L, He T, Ng CF, Wang S, Sun H, Fan HJ. TiO₂/(CdS, CdSe, CdSeS) nanorod heterostructures and photoelectrochemical properties. *J Phys Chem C.* 2012;116(22):11956.
 - [30] Mohapatra SK, Banerjee S, Misra M. Synthesis of Fe₂O₃/TiO₂ nanorod-nanotube arrays by filling TiO₂ nanotubes with Fe. *Nanotechnology.* 2008;19(31):315601.
 - [31] Barreca D, Carraro G, Gasparotto A, Maccato C, Warwick MEA, Kaunisto K, Sada C, Turner S, Gönüllü Y, Ruoko TP, Borgese L, Bontempi E, Tendeloo GV, Lemmetyinen H, Mathur S. Fe₂O₃-TiO₂ nano-heterostructure photoanodes for highly efficient solar water oxidation. *Adv Mater Interfaces.* 2015;2(17):1500313.
 - [32] Luan SL, Qu D, An L, Jiang WS, Gao X, Hua SX, Miao X, Wen YJ, Sun ZC. Enhancing photocatalytic performance by constructing ultrafine TiO₂ nanorods/g-C₃N₄ nanosheets heterojunction for water treatment. *Sci Bull.* 2018;63(11):683.
 - [33] Konta R, Ishii T, Kato H, Kudo A. Photocatalytic activities of noble metal ion doped SrTiO₃ under visible light irradiation. *J Phys Chem B.* 2004;108(26):8992.
 - [34] Xie TH, Sun X, Lin J. Enhanced photocatalytic degradation of RhB driven by visible light-induced MMCT of Ti(IV)-O-Fe(II) formed in Fe-doped SrTiO₃. *J Phys Chem C.* 2008;112(26):9753.
 - [35] Chen HC, Huang CW, Wu JCS, Lin ST. Theoretical Investigation of the metal-doped SrTiO₃ photocatalysts for water splitting. *J Phys Chem C.* 2012;116(14):7897.
 - [36] Liu JW, Chen G, Li ZH, Zhang ZG. Electronic structure and visible light photocatalysis water splitting property of chromium-doped SrTiO₃. *J Solid State Chem.* 2006;179(12):3704.
 - [37] Liu Y, Xie L, Li Y, Yang R, Qu J, Li Y, Li X. Synthesis and high photocatalytic hydrogen production of SrTiO₃ nanoparticles from water splitting under UV irradiation. *J Power Sources.* 2008;183(2):701.
 - [38] Wang M, Zheng D, Ye M, Zhang C, Xu B, Lin C, Sun L, Lin Z. One-dimensional densely aligned perovskite-decorated semiconductor heterojunctions with enhanced photocatalytic activity. *Small.* 2015;11(12):1436.
 - [39] Zhang J, Bang JH, Tang C, Kamat PV. Tailored TiO₂-SrTiO₃ heterostructure nanotube arrays for improved photoelectrochemical performance. *ACS Nano.* 2010;4(1):387.
 - [40] Kim TW, Choi KS. Nanoporous BiVO₄ photoanodes with dual-layer oxygen evolution catalysts for solar water splitting. *Science.* 2014;343(6174):990.
 - [41] Neville RC, Hoeneise B, Mead CA. Permittivity of strontium titanate. *J Appl Phys.* 1972;43(5):2124.
 - [42] Tobar ME, Krupka J, Ivanov EN, Woode RA. Anisotropic complex permittivity measurements of mono-crystalline rutile between 10 and 300 K. *J Appl Phys.* 1998;83(3):1604.
 - [43] Burnside S, Moser JE, Brooks K, Gratzel M, Cahen D. Nanocrystalline mesoporous strontium titanate as photoelectrode material for photosensitized solar devices: increasing photovoltage through flatband potential engineering. *J Phys Chem B.* 1999;103(43):9328.